


# SCIENTIFIC REPORTS



OPEN

## Controllable Phase Transformation and Mid-infrared Emission from $\text{Er}^{3+}$ -Doped Hexagonal-/Cubic- $\text{NaYF}_4$ Nanocrystals

Received: 13 May 2016

Accepted: 23 June 2016

Published: 25 July 2016

Dandan Yang<sup>1</sup>, Dongdan Chen<sup>1</sup>, Huilin He<sup>1</sup>, Qiwen Pan<sup>1</sup>, Quanlan Xiao<sup>2</sup>, Jianrong Qiu<sup>1</sup> & Guoping Dong<sup>1</sup>

The morphology of hexagonal phase  $\text{NaYF}_4:\text{Er}^{3+}$  nanorods synthesized by hydrothermal method changed greatly after a continuing calcination, along with a phase transformation to cubic phase. Photoluminescence (PL) spectra indicated that mid-infrared (MIR) emission was obtained in both hexagonal and cubic phase  $\text{NaYF}_4:\text{Er}^{3+}$  nanocrystals for the first time. And the MIR emission of  $\text{NaYF}_4:\text{Er}^{3+}$  nanocrystals enhanced remarkably at higher calcination temperature. To prevent uncontrollable morphology from phase transformation, the cubic phase  $\text{NaYF}_4:\text{Er}^{3+}$  nanospheres with an average size of  $\sim 100$  nm were prepared *via* a co-precipitation method directly. In contrast, the results showed better morphology and size of cubic phase  $\text{NaYF}_4:\text{Er}^{3+}$  nanocrystals have realized when calcined at different temperatures. And PL spectra demonstrated a more intense MIR emission in the cubic phase  $\text{NaYF}_4:\text{Er}^{3+}$  nanocrystals with an increasing temperature. Besides, the MIR emission peak of  $\text{Er}^{3+}$  ions had an obvious splitting in cubic phase  $\text{NaYF}_4$ . Therefore, cubic phase  $\text{NaYF}_4:\text{Er}^{3+}$  nanospheres with more excellent MIR luminescent properties seems to provide a new material for nanocrystal-glass composites, which is expected to open a broad new field for the realization of MIR lasers gain medium.

Mid-infrared (MIR) fiber lasers operating at  $\sim 3 \mu\text{m}$  are in great demand for a variety of applications including medical surgery, hazardous chemical detection, remote sensing, eye safe laser radar and atmosphere pollution monitoring<sup>1–5</sup>. This mainly relies on the two unique features of this wavelength range: (1) well-known atmospheric transparency windows are located in this wavelength range; (2) various molecules have strong rovibronic absorption lines in this ‘molecular fingerprint’ region of the electromagnetic spectrum<sup>1</sup>. So far, glass-based materials (conventional glass and glass ceramics materials) may be the most important material used for optical fiber production<sup>6–8</sup>. However, MIR emission at  $\sim 3 \mu\text{m}$  is the closely spaced energy levels transition, which is liable to be quenched by multiphonon non-radiative decay, hence, it seems difficult to obtain intense MIR emission in most glass-based materials. In comparison with glass-based materials, nanocrystal (NC) materials are thought to be more suitable as MIR laser host because of their many advantages with smaller particle size, higher chemical stability, more nature synthesis method, lower thermal lens effect and higher doping concentration of trivalent rare-earth (RE) ions<sup>9–13</sup>. Thus, in our previous work<sup>11</sup>, a novel co-melting technology has been proposed to introduce RE ions doped NC into glass matrixes to form NC-doped glass composite (NGC). The NGC can provide a stable crystalline field for active ion to realize higher MIR luminescent efficiency, and have potential for fiber-drawing, which will open a brand new field for the realization of MIR fiber lasers.

NGC and co-melting technology present a new approach to research the MIR composite optical fiber pre-forms and fiber forming. However, the preparation of NGC brings forward rigorous demands to the MIR emission NCs, such as high MIR luminescent intensity, controllable morphology and better thermal stability etc. So it is extremely important to search suitable MIR emission NCs for NGC preparation. As an ideal host, fluorides

<sup>1</sup>State Key Laboratory of Luminescent Materials and Devices and Institute of Optical Communication Materials, School of Materials Science and Engineering, South China University of Technology, Guangzhou 510640, China. <sup>2</sup>SZU-NUS Collaborative Innovation Center for Optoelectronic Science & Technology, Key Laboratory of Optoelectronic Devices and Systems of Ministry of Education and Guangdong Province, College of Optoelectronic Engineering, Shenzhen University, Shenzhen 518060, China. Correspondence and requests for materials should be addressed to G.D. (email: dgp@scut.edu.cn)

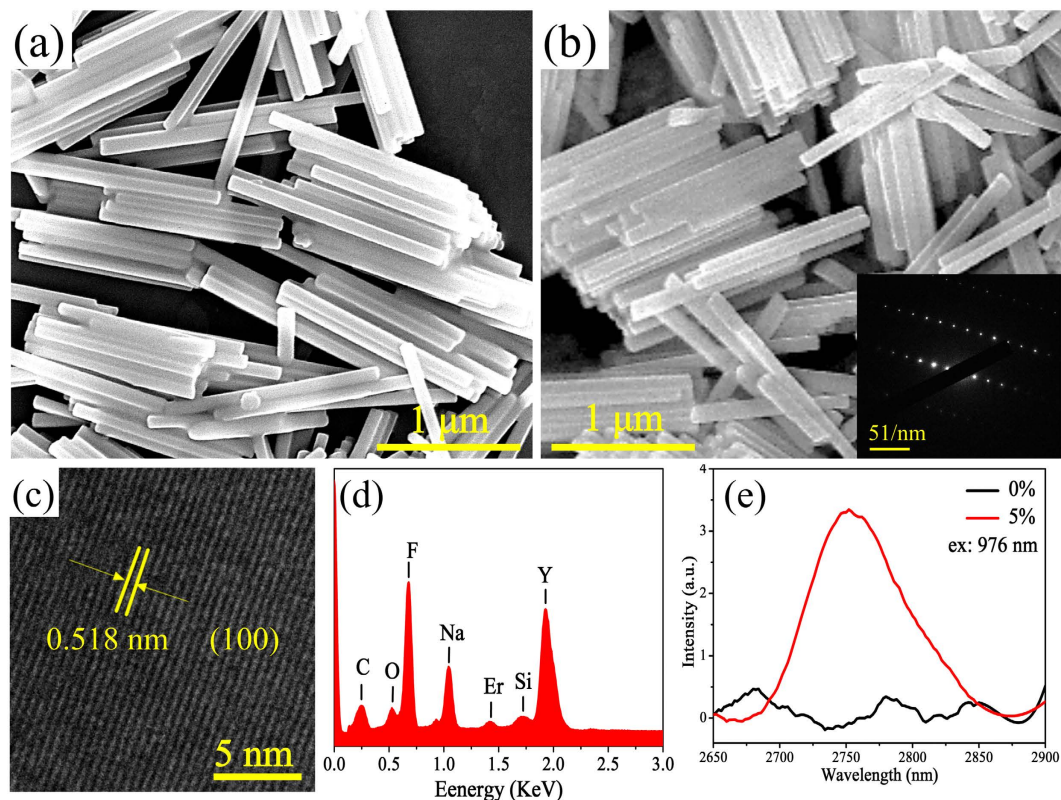


**Figure 1.** (a,b) SEM images of the as-prepared  $\beta$ -NaYF<sub>4</sub> and  $\beta$ -NaYF<sub>4</sub>:5%Er<sup>3+</sup> nanocrystals. (c) HRTEM image and (d) EDS spectrum of as-prepared  $\beta$ -NaYF<sub>4</sub>:5%Er<sup>3+</sup> nanocrystals. (e) The MIR emission spectra of as-prepared  $\beta$ -NaYF<sub>4</sub> and  $\beta$ -NaYF<sub>4</sub>:5%Er<sup>3+</sup> nanocrystals. The inset in (b) is corresponding SAED pattern.

with low phonon frequency and intense crystalline field, have been widely studied<sup>14–16</sup>. Among these RE fluorides, NaYF<sub>4</sub> with low vibration energy ( $<400\text{ cm}^{-1}$ )<sup>17</sup>, controllable morphology and particle size<sup>18</sup> have attracted widespread attention to study the visible up-conversion and near-infrared emission of RE ions in NaYF<sub>4</sub> NCs<sup>17–21</sup>. To our best knowledge, no any works are reported about the MIR emission in RE-doped NaYF<sub>4</sub> NCs yet. In consideration of the above superiorities, NaYF<sub>4</sub> NCs are thought to be one of the best MIR luminescent host and chosen as the host material in this work. There are two kinds of NaYF<sub>4</sub> host material: cubic ( $\alpha$ ) and hexagonal ( $\beta$ ) phases. At present, a number of methods have been available to synthesize these two kinds of NaYF<sub>4</sub> NCs, including solid treatment, co-precipitation method, hydrothermal/solvothermal synthesis and the surfactant-controlled organometallic pyrolysis approach<sup>17–19</sup>. In this work, environment friendly hydrothermal and co-precipitation methods are chosen to prepare the two kinds of NaYF<sub>4</sub> host material, respectively.

Up to now, numerous RE ions in suitable host have realized the MIR emission, such as Er<sup>3+</sup>, Ho<sup>3+</sup> and Dy<sup>3+</sup><sup>22–24</sup>. Among them, Er<sup>3+</sup> emission at 2.7  $\mu\text{m}$  attributed to the  ${}^2I_{11/2} \rightarrow {}^4I_{13/2}$  transition, plays an important role in the investigations and has been achieved in many kinds of glasses<sup>25,26</sup>, glass ceramics<sup>27,28</sup> and single crystals<sup>29</sup>. Hence, in this paper, utilizing Er<sup>3+</sup> ions as active centre, Er<sup>3+</sup>-doped NaYF<sub>4</sub> NCs with intense MIR fluorescence was investigated, which is expected to be used as gain medium of MIR fiber laser.

## Results

**Structures, morphologies and fluorescence of  $\beta$ -NaYF<sub>4</sub>:5%Er<sup>3+</sup> NCs.** Using hydrothermal synthesis, pure hexagonal phase NaYF<sub>4</sub> NCs was fabricated, as shown in XRD patterns in Supplementary Fig. S1. After the substitution of Y<sup>3+</sup> ions by 5% Er<sup>3+</sup> ions, there is no influence on crystal structure. Examining the XRD patterns carefully, it can be noted that (110) crystal facets has higher diffraction intensity than the (101) crystal facets in as-prepared NCs, indicating anisotropic growth along *c*-axis during the synthesis process, which can be proved by the SEM results. It can be seen in Fig. 1(a), all of the as-prepared  $\beta$ -NaYF<sub>4</sub> samples are well-dispersed nanorods with  $\sim 100\text{ nm}$  in width as well as  $\sim 1.3\text{ }\mu\text{m}$  in length. The morphology remains monodisperse nanorods with the similar size after the doping of Er<sup>3+</sup> ions (Fig. 1(b)). The insert in Fig. 1(b) reveals the selected area electron diffraction (SAED) pattern of a single  $\beta$ -NaYF<sub>4</sub>:5%Er<sup>3+</sup> nanorod, which indicates the single  $\beta$ -NaYF<sub>4</sub>:5%Er<sup>3+</sup> nanorod exhibits a single crystalline character. In HRTEM image of a single  $\beta$ -NaYF<sub>4</sub>:5%Er<sup>3+</sup> nanorod (Fig. 1(c)), a series of crystal facets with the spacing value of  $\sim 0.518\text{ nm}$  is observed, which corresponds to the (100) crystal facet of  $\beta$ -NaYF<sub>4</sub> crystals. Therefore, it can be deduced that the addition of Er<sup>3+</sup> ions has no obvious effect on the phase, size and morphology of  $\beta$ -NaYF<sub>4</sub> NCs. Fig. 1(d) describes the EDS spectrum of  $\beta$ -NaYF<sub>4</sub>:5%Er<sup>3+</sup> NCs. The peaks assigned to designed elements (i.e. Na, Y, F and Er) are clearly observed in this picture. Besides,

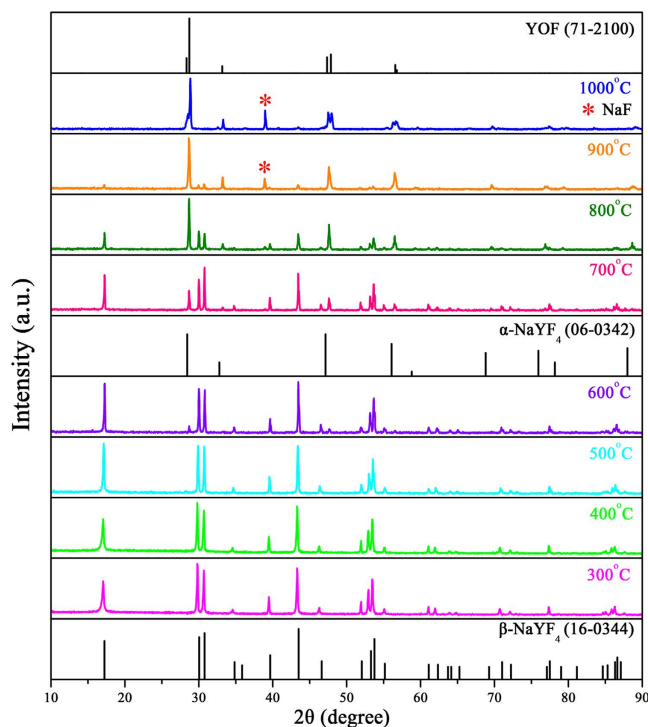


**Figure 2.** XRD patterns of  $\beta$ - $\text{NaYF}_4$ :5% $\text{Er}^{3+}$  nanocrystals calcined at different temperatures for 2 h.

the O, C and Si elements were introduced during the synthesis and measurement process. It is believed that the  $\beta$ - $\text{NaYF}_4$ :5% $\text{Er}^{3+}$  NCs are mainly consisted of Na, Y, F and Er elements.

The MIR emission spectrum of  $\text{Er}^{3+}$  ions doped  $\beta$ - $\text{NaYF}_4$  NCs is shown in Fig. 1(e). Under 976 nm laser diode (LD) pumping, an obvious MIR emission peak at  $\sim 2.75 \mu\text{m}$  attributed to the  $\text{Er}^{3+}$ :  $^4\text{I}_{11/2} \rightarrow ^4\text{I}_{13/2}$  transition is observed in  $\beta$ - $\text{NaYF}_4$  NCs. However, the existence of organic ligands such as  $\text{OH}^-$  etc. (Supplementary Fig. S6), which have a strong absorption at around  $\sim 3 \mu\text{m}$ , can greatly reduce the MIR emission intensity of  $\text{Er}^{3+}$  ions. Therefore, in this study, a convenient method, heat treatment at different temperatures in air atmosphere, was chosen to remove the organic ligands. This is because at high temperature, the organic ligands would volatilize, and  $\text{F}^-$  ions also have hydroscopic property.

**Thermal treatment of  $\beta$ - $\text{NaYF}_4$ :5% $\text{Er}^{3+}$  NCs.** In order to remove organic ligands and realize intense MIR emission, the  $\beta$ - $\text{NaYF}_4$ :5% $\text{Er}^{3+}$  NCs were calcined at different temperatures for 2 h. The  $\beta$ - $\text{NaYF}_4$ : $\text{Er}^{3+}$  NCs calcined at series of temperatures are labeled as B-NYF, and B-NYF-X (X = 300, 400, ..., 1000) represents the B-NYF of corresponding temperature. The crystal structures of B-NYF are displayed in Fig. 2. As shown in this pattern, samples remain pure hexagonal phase less than 600 °C. At 600 °C, an obvious phase transformation from hexagonal to cubic has occurred. When the temperature reaches 900 °C, nearly all  $\beta$ -crystals transform into  $\alpha$ -crystals, while the residual  $\beta$ -crystals could be neglected. Except for  $\text{NaYF}_4$ , a small number of NaF (JCPDF: 36–1455) is detected at this temperature along with the diffraction peaks shift slightly to higher  $2\theta$  region. Further increase of temperature results in the occurrence of rhombohedral phase YOF (JCPDF: 71–2100), which is due to the fact that oxygen atoms in the environment obtain energy entering into crystal lattice to replace fluorine atoms. Thus, the increase of temperature from 300 °C to 1000 °C leads to two phase transformation processes, one is from  $\beta$ - $\text{NaYF}_4$  to  $\alpha$ - $\text{NaYF}_4$ , and the other is the oxidation from  $\alpha$ - $\text{NaYF}_4$  to YOF. Moreover, it is noteworthy that the diffraction peaks of all samples have narrow full width at half maximum (FWHM), indicating the growth of crystalline particles has better crystallinity, which is benefit for fluorescence emission.

It has been reported that the unique Raman peaks can be efficiently used to distinguish cubic and hexagonal phases of  $\text{NaYF}_4$ <sup>30</sup>. So Raman analysis (Supplementary Fig. S2) was used to further prove the XRD results. When calcined less than 600 °C, only dominant Raman peaks of  $\beta$ - $\text{NaYF}_4$ :5% $\text{Er}^{3+}$  NCs are detected<sup>31–33</sup>. At 600 °C, two other weak Raman peaks which attributed to the vibrations from the  $\alpha$ - $\text{NaYF}_4$  appear<sup>30</sup>. With the increase of temperature, the peaks of  $\beta$ - $\text{NaYF}_4$  get weak, and the peaks of  $\alpha$ - $\text{NaYF}_4$  become strong. Until 900 °C, the peaks of hexagonal phase can be ignored comparing with cubic phase. At same time, three new Raman peaks are observed, owing to the vibrations from YOF<sup>34</sup> and NaF. When the temperature reaches 1000 °C, there are only Raman peaks of YOF, NaF and  $\alpha$ - $\text{NaYF}_4$  observed, without peaks of  $\beta$ - $\text{NaYF}_4$ . Above results match well with the XRD patterns, indicating the occurrence of two phase transformation during the calcination process of  $\beta$ - $\text{NaYF}_4$ :5% $\text{Er}^{3+}$  NCs. According to the thermogravimetry-differential scanning calorimetry (TG-DSC) curves (Supplementary Fig. S3), these two phase transformation processes occur at 698.9 and 984 °C, respectively. Due to the fast heating rate and short holding time during the TG-DSC measurement, a slight difference is found between TG-DSC curves and XRD patterns.

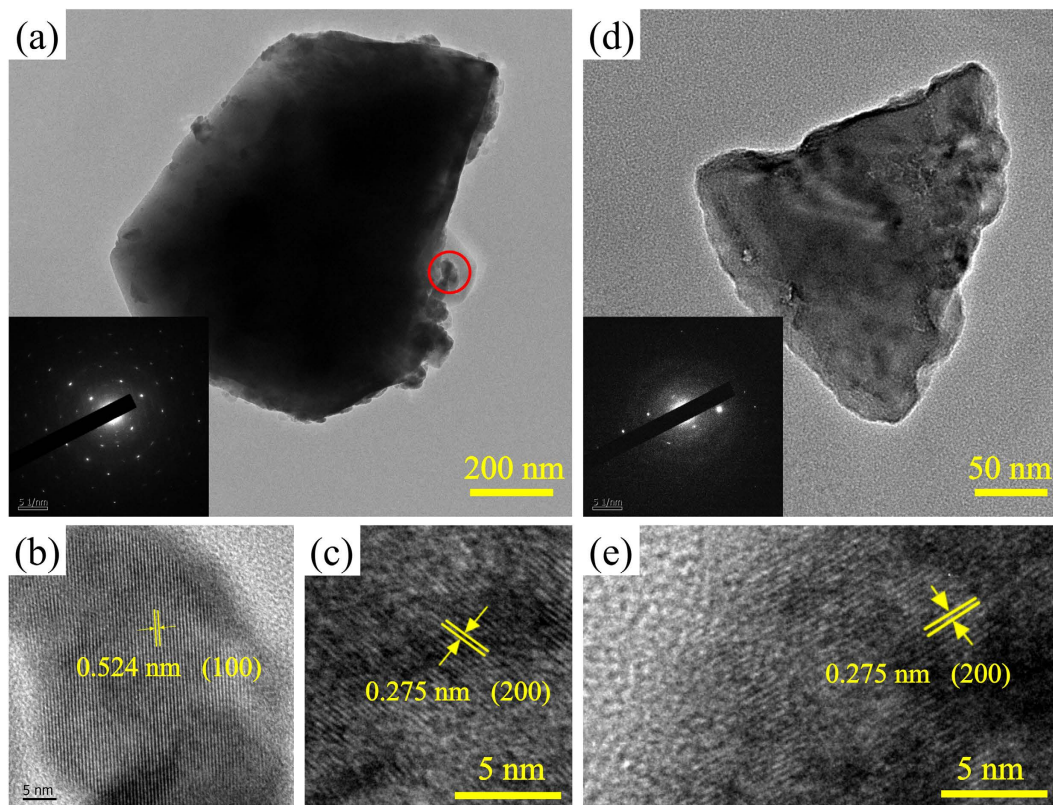


**Figure 3.** (a) TEM image of  $\beta$ - $\text{NaYF}_4$ :5% $\text{Er}^{3+}$  nanocrystals calcined at 700 °C for 2 h. (b,c) HRTEM images of the little particle in red circle and the micro blocks in (a), respectively. (d) TEM image of  $\alpha$ - $\text{NaYF}_4$ :5% $\text{Er}^{3+}$  nanocrystals calcined at 700 °C for 2 h. (e) HRTEM image of samples in (d). The inserts in (a,d) are corresponding SAED pattern.

As displayed in the SEM images of  $\beta$ - $\text{NaYF}_4$ :5% $\text{Er}^{3+}$  NCs calcined at different temperatures (Supplementary Fig. S4), during the process of temperature rise, the morphology has an obvious change, along with crystalline phase transformation from pure  $\beta$ - $\text{NaYF}_4$  to  $\alpha$ - $\text{NaYF}_4$ . The detailed morphology and structure of representative B-NYF-700 samples are shown in Fig. 3(a–c). From Fig. 3(a), it can be seen that the B-NYF-700 samples consist of two kinds of morphologies, micro blocks and little irregular particles. Their corresponding HRTEM images indicate the irregular particles are  $\beta$ - $\text{NaYF}_4$  crystals, and the micro blocks are  $\alpha$ - $\text{NaYF}_4$  crystals. This is because crystal lattice fringe with spacing  $d$  value of  $\sim 0.524$  nm in Fig. 3(b) corresponds to the (100) crystal facets of  $\beta$ - $\text{NaYF}_4$ , and  $\sim 0.275$  nm in Fig. 3(c) matches with the (200) crystal facets spacing of  $\alpha$ - $\text{NaYF}_4$ . As a result, the corresponding SAED pattern reveals polycrystalline character. For B-NYF-1000 samples, there are mainly three kinds of morphologies observed in Supplementary Fig. S5(a,b): nanoplates, irregular nanoparticles and micro blocks. In Supplementary Fig. S5(c), the crystal facets spacing of  $\sim 0.265$  nm corresponds to (111) crystal facets of NaF. And the EDS spectrum (Supplementary Fig. S5(g)) illustrates the nanoplates mainly consist of Na and F elements. So it can be inferred the thin nanoplates are NaF plates. In Supplementary Fig. S5(d,e), the  $\sim 0.318$  nm and  $\sim 0.328$  nm are the crystal lattice fringes of (006) and (101) crystal facets in YOF crystal, which reveals these two kinds of particles are YOF crystals. Therefore, B-NYF-1000 samples consist of three morphologies: NaF nanoplates, YOF irregular nanoparticles and micro blocks.

Based on above results, it can be inferred that B-NYF samples are located in stable state, and remain their original morphology and crystal structure at low temperature ( $< 600$  °C). When calcined at 500 °C,  $\beta$ - $\text{NaYF}_4$  NCs obtain energy and start to fuse slightly. But this temperature is too low to provide enough energy for the phase transformation from hexagonal to cubic phase. Once rising temperature to 600 °C, the energy is enough to fuse  $\beta$ - $\text{NaYF}_4$  NCs thoroughly and form  $\alpha$ - $\text{NaYF}_4$  crystals. At higher temperature,  $\alpha$ - $\text{NaYF}_4$  crystals as high temperature phase gain more energy to nucleate and growth in quantity. Nevertheless, the absence of shaping and stabilizing agents leads to the uncontrollable growth of  $\alpha$ - $\text{NaYF}_4$  crystal nucleus. When the temperature reaches to 1000 °C, the energy is too high so that oxygen atoms in air obtain energy to entire into the crystal lattice and replace fluorine atoms. Finally,  $\alpha$ - $\text{NaYF}_4$  crystal transforms into YOF phase. As for the replaced fluorine atoms, some of them are volatilized, and the remainders combine with sodium atoms to form NaF.

The MIR emission spectra of  $\beta$ - $\text{NaYF}_4$ :5% $\text{Er}^{3+}$  NCs calcined at different temperatures for 2 h is illustrated in Fig. 4. And the inset is enlarged image of  $\beta$ - $\text{NaYF}_4$ :5% $\text{Er}^{3+}$  NCs calcined from 0 to 600 °C for 2 h. It is found that, at higher temperature, an intense MIR emission is detected. But, at lower temperature, B-NYF samples have weaker MIR emission than that of as-prepared samples. This is because the combustion and volatilization of organic ligands would introduce numerous defects on the surface of  $\beta$ - $\text{NaYF}_4$ :5% $\text{Er}^{3+}$  NCs, and these defects could greatly

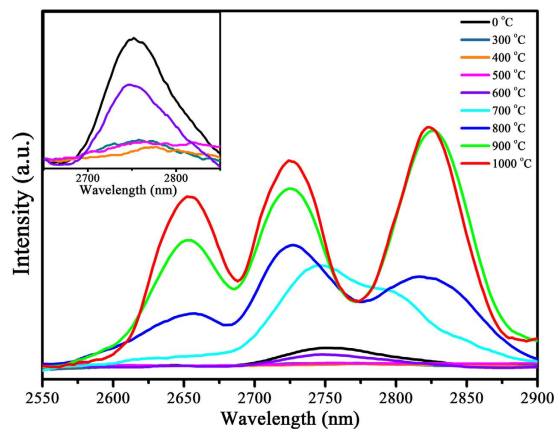


**Figure 4.** MIR emission spectra of  $\beta$ -NaYF<sub>4</sub>:5%Er<sup>3+</sup> nanocrystals calcined at different temperatures for 2 h. Inset: the enlarged image of the curves of  $\beta$ -NaYF<sub>4</sub>:5%Er<sup>3+</sup> nanocrystals (calcined from 0 to 600 °C for 2 h) in the range from 2650 nm to 2850 nm, respectively. The 0 °C stands for as-prepared  $\beta$ -NaYF<sub>4</sub>:5%Er<sup>3+</sup> nanocrystals.

quench  $\sim 2.7$   $\mu$ m fluorescence of Er<sup>3+</sup> ions<sup>35</sup>. According to FTIR spectra (Supplementary Fig. S6) and TG-DSC curves (Supplementary Fig. S3), it can be noted that, more organic ligands combust and volatilize at 400 °C than at 300 °C, so B-NYF-400 samples contain more defects when they have similar morphology. Accordingly, weaker MIR emission was detected in B-NYF-400 samples. From 400 to 600 °C, the fusion and agglomeration of samples decrease some surface defects, as a result, an increasing MIR emission intensity was observed. From 700 °C, a noticeable enhancement of MIR emission in B-NYF samples with the increase of temperature can be ascribed into three main reasons as follows. Firstly, recrystallization from hexagonal NCs into cubic micro blocks efficiently reduces the defects, including surface defects and internal defects. The surface defects can greatly quench MIR emission, and the internal defects coming from phase transformation can transfer excitation energy to trap level by nonradiative relaxation to reduce pumping efficiency<sup>36</sup>. Secondly, the  $\alpha$ -NaYF<sub>4</sub> micro blocks have more excellent crystallinity at higher temperature. Thirdly, the FTIR spectra (Supplementary Fig. S6) show the organic ligands in the structure of B-NYF samples have been removed thoroughly upon 600 °C. In these spectra, it is worth mentioning that the emission peak appears splitting along with formation of cubic phase.

In conclusion, at high temperature, especially 900 °C, MIR fluorescence of Er<sup>3+</sup> ions with high intensity was achieved in B-NYF samples. However, the transformation from  $\beta$ -NaYF<sub>4</sub> NCs to irregular  $\alpha$ -NaYF<sub>4</sub> micro blocks would extremely limit their application. Hence, in order to prevent  $\beta$ -NaYF<sub>4</sub> NCs transform into  $\alpha$ -NaYF<sub>4</sub> micro blocks at 700 °C, and avoid phase transformation ( $\beta \rightarrow \alpha$ ) during the calcination process,  $\alpha$ -NaYF<sub>4</sub>:5%Er<sup>3+</sup> NCs were prepared as precursors directly, and then calcined at different temperatures for 2 h in air. It is expected that  $\alpha$ -NaYF<sub>4</sub>:5%Er<sup>3+</sup> NCs can remain original crystal phase and controllable morphology as well as size after calcination.

**Structures, morphologies and fluorescence of  $\alpha$ -NaYF<sub>4</sub>:5%Er<sup>3+</sup> NCs.** Utilizing Na<sub>2</sub>EDTA as precipitator, pure cubic phase NaYF<sub>4</sub>:5%Er<sup>3+</sup> NCs were obtained *via* co-precipitation method, as shown in XRD patterns in Supplementary Fig. S7. The morphology of as-prepared crystals is described in Fig. 5(a,b). In Fig. 5(a), the as-prepared undoped  $\alpha$ -NaYF<sub>4</sub> sample consists of a large quantity of uniform, monodisperse and spherical particles with diameter of  $\sim 100$  nm. When replacing 5%Y<sup>3+</sup> ions with Er<sup>3+</sup> ions, there is no influence on the morphology. The insert in Fig. 5(b) is TEM image of a single  $\alpha$ -NaYF<sub>4</sub>:5%Er<sup>3+</sup> nanoparticle, which reveals the single  $\alpha$ -NaYF<sub>4</sub>:5%Er<sup>3+</sup> nanoparticle is spherical. Further crystal structure and component analysis of as-prepared  $\alpha$ -NaYF<sub>4</sub>:5%Er<sup>3+</sup> NCs are characterized in Fig. 5(c–e). The SAED pattern shows the single crystalline character of the individual  $\alpha$ -NaYF<sub>4</sub>:5%Er<sup>3+</sup> nanosphere. In the HRTEM image, the clear crystal lattice fringes with the spacing  $d$  values of  $\sim 0.313$  nm and  $\sim 0.281$  nm correspond to the (111) and (200)  $d$ -spacing of  $\alpha$ -NaYF<sub>4</sub>. In EDS spectrum (Fig. 5(e)), except for peaks assigned to designed elements (i.e. Na, Y, F and Er) as well as the elements introduced during the synthesis and measurement process (O, C, Cu and Si), no other impurity is detected.

Similar to  $\beta$ -NaYF<sub>4</sub>:5%Er<sup>3+</sup> NCs, as-prepared  $\alpha$ -NaYF<sub>4</sub>:5%Er<sup>3+</sup> NCs were calcined at different temperatures to remove organic ligands. For  $\beta$ -NaYF<sub>4</sub>:5%Er<sup>3+</sup> NCs, the cubic phase appeared at 600 °C, so 500 °C was selected as beginning temperature for  $\alpha$ -NaYF<sub>4</sub>:5%Er<sup>3+</sup> NCs. The  $\alpha$ -NaYF<sub>4</sub>:Er<sup>3+</sup> NCs calcined at series of temperatures are labeled as A-NYF, and A-NYF-X (X = 500, 600, ..., 1000) represents the A-NYF of corresponding temperature. Figure 6 shows XRD patterns of A-NYF. It can be noted, at 500 and 600 °C, hexagonal phase still is main phase. Herein, the temperature is hard to reach the required temperature directly during the calcination process, leading to the appearance of low temperature hexagonal phase. However, it can be observed clearly, in contrast to B-NYF samples, a considerable part of cubic phase exists in A-NYF samples at 500 and 600 °C, which indicates that a part of cubic phase NCs do not undergo the phase transformation. From 700 °C, the hexagonal phase forming during calcination process transformed into cubic phase again, and disappeared gradually with temperature rise. At 900 °C, nearly only cubic phase is monitored. As temperature reaches 1000 °C, O atoms gain energy and enter into crystal lattice, resulting in the slight shift of diffraction peaks and formation of NaF. Thus, the increase of temperature from 500 °C to 1000 °C contains two phase transformation processes:  $\alpha \rightarrow \beta$  at lower temperature and  $\beta \rightarrow \alpha$  at higher temperature. This conclusion can be proved by Raman analysis and TG-DSC curves. As shown in

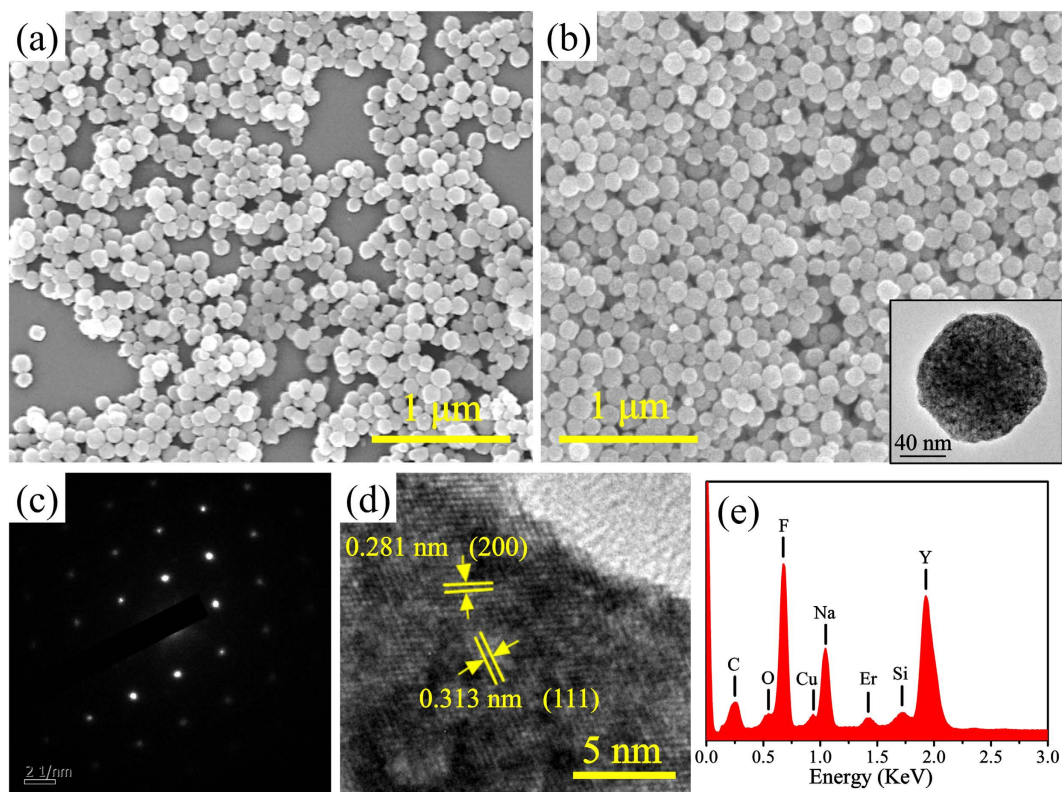


**Figure 5.** (a,b) SEM images of the as-prepared  $\alpha$ -NaYF<sub>4</sub> and  $\alpha$ -NaYF<sub>4</sub>:5%Er<sup>3+</sup> nanocrystals. (c) SAED pattern, (d) HRTEM image and (e) EDS spectrum of as-prepared  $\alpha$ -NaYF<sub>4</sub>:5%Er<sup>3+</sup> nanocrystals, respectively. The insert in (b) is TEM image of a single  $\alpha$ -NaYF<sub>4</sub>:5%Er<sup>3+</sup> nanocrystal.

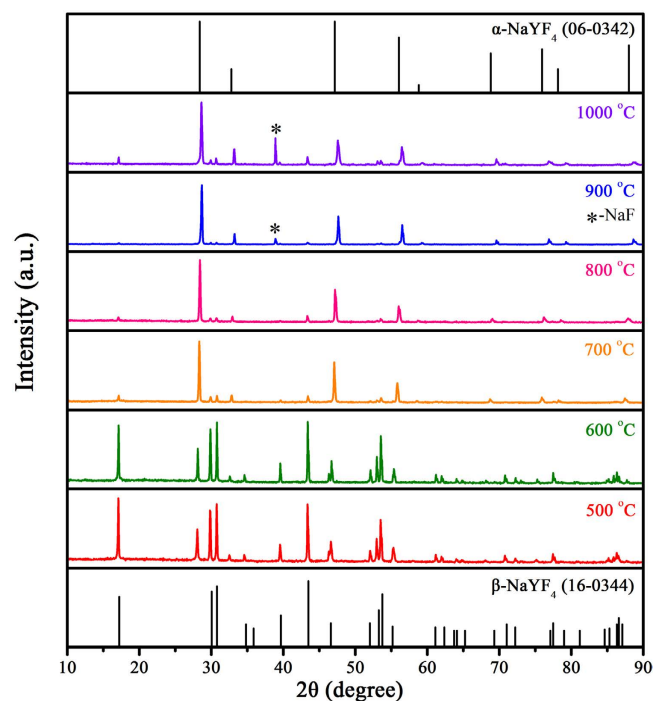


**Figure 6.** XRD patterns of  $\alpha$ -NaYF<sub>4</sub>:5%Er<sup>3+</sup> nanocrystals calcined at different temperatures for 2 h.

Raman spectra (Supplementary Fig. S8), the Raman peaks of hexagonal phase can be detected from 500 °C, and decrease gradually along with the increase of temperature. Until 900 °C, nearly only Raman peaks of cubic phase,

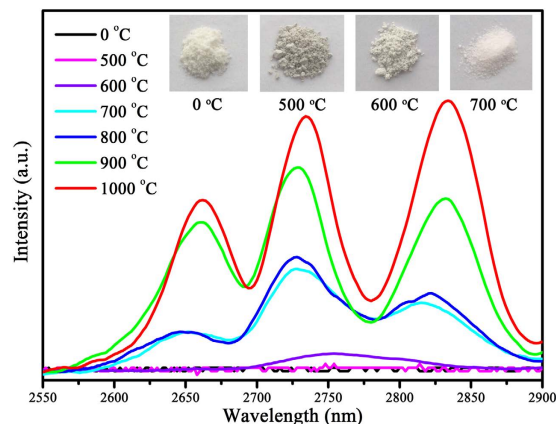


**Figure 7.** MIR emission spectra of  $\alpha$ - $\text{NaYF}_4$ :5% $\text{Er}^{3+}$  nanocrystals calcined at different temperatures for 2 h. Inset: sample photos of  $\alpha$ - $\text{NaYF}_4$ :5% $\text{Er}^{3+}$  nanocrystals calcined at different temperatures for 2 h. The 0 °C stands for as-prepared  $\alpha$ - $\text{NaYF}_4$ :5% $\text{Er}^{3+}$  nanocrystals.

YOF and NaF are monitored. On the basis of TG-DSC curves in Supplementary Fig. S9, three phase transformation temperatures are confirmed: cubic phase transformed into hexagonal phase at  $\sim 480$  °C, then hexagonal phase transformed back cubic phase at  $\sim 692$  °C, finally  $\text{NaYF}_4$  was oxidized into YOF upon 1000 °C.

The SEM images of A-NYF are shown in Supplementary Fig. S10. Similar with  $\beta$ - $\text{NaYF}_4$ :5% $\text{Er}^{3+}$  NCs, the nanospheres change into bigger irregular nano-blocks after continuous calcination because of the phase transformation process. Based on the TEM results, the detailed morphology and structure of representative A-NYF samples are illustrated in Fig. 3(d). The insert is the corresponding SAED pattern, which describes the single crystalline character of the nano-blocks. The HRTEM image is displayed in Fig. 3(e), in which a crystal lattice fringe with the spacing  $d$  value of  $\sim 0.273$  nm corresponds to the (200) crystal facet of  $\alpha$ - $\text{NaYF}_4$ . Consequently, it can be deduced, when  $\alpha$ - $\text{NaYF}_4$ :5% $\text{Er}^{3+}$  NCs were calcined at different temperatures, some samples would transform into hexagonal phase at low temperature, giving rise to fusion and agglomeration of samples. From 700 °C, all samples obtain enough energy to fuse thoroughly and agglomerate to irregular nano-blocks. And just a few  $\beta$ - $\text{NaYF}_4$  samples dispersed among the nano-blocks, which are difficult to be observed. It is important to emphasize that it is difficult to achieve completely controllable morphology for  $\alpha$ - $\text{NaYF}_4$ :5% $\text{Er}^{3+}$  NCs, but compared to B-NYF samples (Supplementary Fig. S4), A-NYF samples treated from 700 °C present pure cubic phase, smaller particle size, better uniformity and dispersibility. Accordingly,  $\alpha$ - $\text{NaYF}_4$ :5% $\text{Er}^{3+}$  NCs seem have more potential to combine with glass forming NGC.

MIR emission spectra of  $\alpha$ - $\text{NaYF}_4$ :5% $\text{Er}^{3+}$  NCs calcined at different temperatures for 2 h is revealed in Fig. 7. It is worth noting that, there is no MIR emission from as-prepared  $\alpha$ - $\text{NaYF}_4$ :5% $\text{Er}^{3+}$  NCs, which can be explained as follows: (1) the  $\text{OH}^-$  in the structure of as-prepared  $\alpha$ - $\text{NaYF}_4$ :5% $\text{Er}^{3+}$  NCs have greatly absorbed MIR emission of  $\text{Er}^{3+}$  ions (Supplementary Fig. S11); (2) according to Raman analysis (Supplementary Fig. S8), the poor crystallinity of as-prepared  $\alpha$ - $\text{NaYF}_4$ :5% $\text{Er}^{3+}$  NCs induces that there is no MIR emission of  $\text{Er}^{3+}$  ions; (3) the smaller size and bigger specific surface area of the as-prepared  $\alpha$ - $\text{NaYF}_4$ :5% $\text{Er}^{3+}$  NCs introduce more surface defects, which can quench MIR emission of  $\text{Er}^{3+}$  ions seriously. When  $\alpha$ - $\text{NaYF}_4$ :5% $\text{Er}^{3+}$  NCs calcined at 500 °C, just as B-NYF, A-NYF samples contain many inner defects and surface defects. The former is attributed to the phase transformation from cubic to hexagonal, and the latter is owing to volatilization of organic ligands. Besides, it can be found in FTIR pattern (Supplementary Fig. S11) and the insert in Fig. 7, the carbonization of organic ligands in as-prepared  $\alpha$ - $\text{NaYF}_4$ :5% $\text{Er}^{3+}$  NCs leads the products become black, which can efficiently absorb excitation and emission luminescence. Consequently, no MIR emission is detected in A-NYF-500 samples. Because of better crystallinity at higher temperature, A-NYF samples treated at 600 °C reveal stronger MIR emission than at 500 °C. Upon 600 °C, A-NYF samples agglomerate into nano-blocks with large size, which can reduce defects greatly. Furthermore, with an increase of temperature, A-NYF samples have more excellent crystallinity. As a result, an obvious enhancement of MIR fluorescence is observed along with the increase of temperature. When temperature reaches 1000 °C, emission peaks have a slight red shift, which may be due to the entrance of some O atoms into crystal structure in the way of replacing F atoms. It is surprising that, the same consequence is also found on A-NYF samples, which is when  $\alpha$  phase as main phase, emission peak has an obvious splitting.

## Discussion

It is well known that, for MIR laser operation, host materials must be non-hygroscopic and characterized by low phonon energy, considering that there is a strong absorption at  $\sim 3$   $\mu\text{m}$  of  $\text{H}_2\text{O}$  molecules, and increase of non-radiative relaxations by high phonon energies can reduce MIR emission remarkably. However, in our study, another two factors show more intense effect on MIR emission of  $\text{Er}^{3+}$  ions. The FTIR results of  $\beta$ - $\text{NaYF}_4$ :5% $\text{Er}^{3+}$  NCs calcined at different temperatures (Supplementary Fig. S6) demonstrate there is no  $\text{OH}^-$  in the structure of B-NYF samples, but weaker MIR emission is detected in B-NYF-300 to  $-600$  samples due to occurrence of defects produced by volatilization of organic ligands and phase transformation. With the increase of temperature, the significantly decreased defects and increased crystallinity result in the gradual enhancement of MIR emission of  $\text{Er}^{3+}$  ions in B-NYF samples. Similarly, A-NYF samples obtained at different temperatures also contain

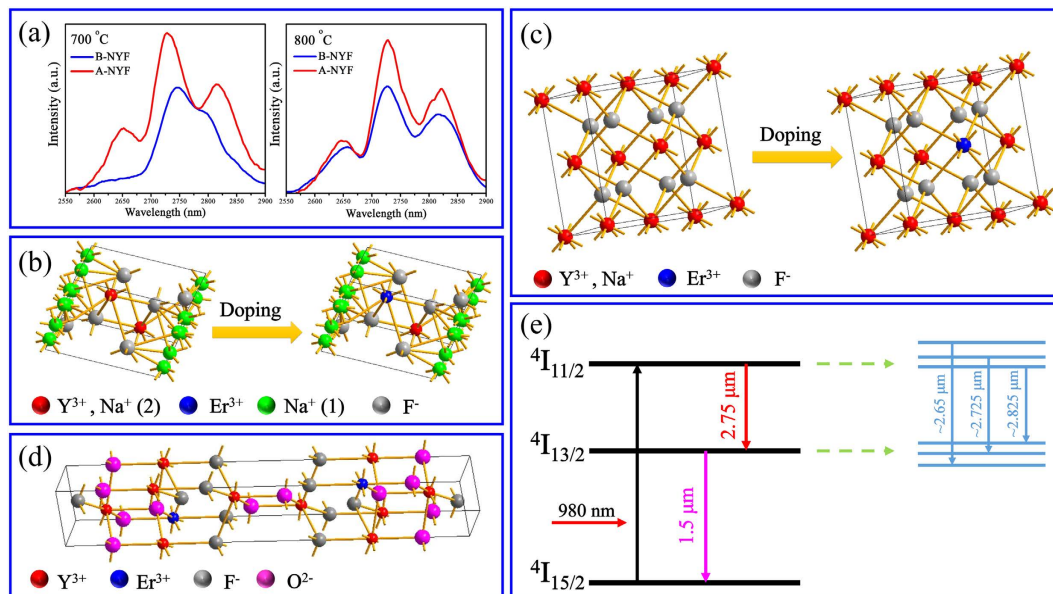


**Figure 8.** (a) The comparison of MIR emission spectra between B-NYF and A-NYF samples obtained at different temperatures. (b,c) Schematic presentation of hexagonal and cubic phase NaYF<sub>4</sub> structures, respectively. (d) The crystal structure of the rhombohedral phase Er<sup>3+</sup>-doped YOF. (e) Energy levels of Er<sup>3+</sup> ions and possible emission pathways of splitting energy levels.

no OH<sup>-</sup> based on its FTIR analysis (Supplementary Fig. S11), but the defects lead to weaker MIR emission in A-NYF-500 and A-NYF-600 samples. From 700 °C, A-NYF samples have an obvious enhancement of MIR emission, which results from the more excellent crystallinity. According to above results, it can be deduced that the defect and crystallinity have more significant influence on the MIR fluorescence of Er<sup>3+</sup> ions in crystal hosts.

Figure 8(a) shows the comparison of MIR emission between B-NYF and A-NYF samples treated at 700 °C and 800 °C. As one can see, A-NYF samples have stronger MIR emission intensity than B-NYF samples. Check their corresponding XRD results (Figs 2 and 6) carefully, more hexagonal phase can be detected in B-NYF samples, which can be neglected in A-NYF samples, leading to more defects and worse crystallinity for B-NYF samples. Based on above results, defect and crystallinity are the main influencing factors for MIR emission of Er<sup>3+</sup> ions in our study, so B-NYF samples display weaker MIR emission. Moreover, it can be noted that NaYF<sub>4</sub> samples with pure hexagonal phase or hexagonal phase as main phase, only have one MIR emission peak at ~2.75 μm, while the emission peak splits into three emission peaks along the appearance of cubic phase. Hence, we deduce Er<sup>3+</sup> ions in cubic phase occur energy level splitting.

Schematic of hexagonal- and cubic-phase NaYF<sub>4</sub> structures are presented in Fig. 8(b,c). In hexagonal phase NaYF<sub>4</sub>, an ordered array of F<sup>-</sup> ions offers two types of cation sites: one occupied by Na<sup>+</sup>, and the other occupied by Y<sup>3+</sup> and Na<sup>+</sup>, so Y<sup>3+</sup> ions are located in nine-coordinated sites with low-symmetry. In contrast, in the crystal structure of cubic phase NaYF<sub>4</sub> containing one type of high-symmetry cation site, fluorite structures (CaF<sub>2</sub>) are formed, with the cation sites randomly occupied by Na<sup>+</sup> and Y<sup>3+</sup>, so Y<sup>3+</sup> ions occupy the eight-coordinated cubic symmetry site<sup>11</sup>. When doping Er<sup>3+</sup> ions into the NaYF<sub>4</sub> crystals, Er<sup>3+</sup> ions will replace Y<sup>3+</sup> ions and occupy its lattice sites, as displayed in Fig. 8(b,c). Therefore, in hexagonal phase, Er<sup>3+</sup> ions are located in a low-symmetry nine-coordinated site, and in cubic phase, Er<sup>3+</sup> ions reside in the eight-coordinated cubic polyhedra with high symmetry. For cubic symmetry, the energy levels of Er<sup>3+</sup> ions can be decomposed into irreducible representations. It has been reported, when Er<sup>3+</sup> ions doped into β-PbF<sub>2</sub> crystal which can offer an eight-coordinated cubic symmetry, the <sup>4</sup>I<sub>15/2</sub> ground energy level and <sup>4</sup>I<sub>13/2</sub> excited energy level of Er<sup>3+</sup> ions all split into multiplet<sup>37,38</sup>. Cubic phase NaYF<sub>4</sub> crystal, owning similar structure with β-PbF<sub>2</sub> crystal, also provides Er<sup>3+</sup> ions an eight-coordinated cubic symmetry, leading to energy level splitting of Er<sup>3+</sup> ions, so there are three MIR emission peaks detected in α-NaYF<sub>4</sub>:5%Er<sup>3+</sup> crystals. For nine-coordinated site, its symmetry is too low to realize Er<sup>3+</sup> ions multiplet emission, so there is only one MIR emission peak detected in hexagonal phase. In rhombohedral phase YOF crystals, Y<sup>3+</sup> ions are coordinated by four oxide and four fluoride anions in a bicapped trigonal antiprism arrangement and all ions (F<sup>-</sup>, O<sup>2-</sup>, and Y<sup>3+</sup>) occupy the six-fold 6c Wyckoff positions with the same C<sub>3v</sub> site symmetry, as shown in Fig. 8(d)<sup>34</sup>. Er<sup>3+</sup> ions in obtained YOF crystals reside in eight-coordinated cubic symmetry, too. Thereby, three MIR splitting peaks were detected in B-NYF-1000 samples. The number of possible Stark levels of each energy is determined by the quantum number of the total angular momentum *J* of the energy level and the number of electrons of the considered ion<sup>39</sup>. Following Kramer's theorem, each energy level splits into a maximum number of Stark levels<sup>37,39–41</sup>, with



$$\begin{cases} 2J + 1 & \text{for an even number of electrons,} \\ \frac{2J + 1}{2} & \text{for an odd number of electrons.} \end{cases} \quad (1)$$

Each  $\text{Er}^{3+}$  ion contains 65 electrons, so that is to say there should be 6 sub-levels for  $^4I_{11/2}$  state and 7 sub-levels for  $^4I_{13/2}$  state theoretically. However, eight-coordinated cubic symmetry is a relatively lower symmetry. Furthermore, due to  $\text{Er}^{3+}$  (0.0881 nm) has smaller ionic radius than  $\text{Y}^{3+}$  (0.0893 nm)<sup>22</sup>, the actual symmetry of  $\text{Er}^{3+}$  ions in these excited-states is slightly lower. In fact,  $\text{Er}^{3+}$  can't achieve complete split when in eight-coordinated site of cubic phase  $\text{NaYF}_4$ , and only three splitting peaks detected for  $\alpha\text{-NaYF}_4:5\%\text{Er}^{3+}$  crystals. Thus, when  $\text{Er}^{3+}$  ions occupy cubic symmetry site in  $\alpha\text{-NaYF}_4$  crystals, the  $^4I_{11/2}$  and  $^4I_{13/2}$  energy levels occur imperfect splitting, and realize MIR emission with three splitting peaks by radiative transition of electrons from sub-levels of  $^4I_{11/2}$  state to sub-levels of  $^4I_{13/2}$  state, as shown in Fig. 8(e). The specific study about level splitting of  $\text{Er}^{3+}$  in  $\alpha\text{-NaYF}_4$  crystal still need further investigation.

In summary, monodisperse  $\beta\text{-NaYF}_4:5\%\text{Er}^{3+}$  nanorods and  $\alpha\text{-NaYF}_4:5\%\text{Er}^{3+}$  nanospheres were synthesized by hydrothermal and co-precipitation method, respectively. For the first time, MIR emission attributed to radiative transition from  $^4I_{11/2}$  to  $^4I_{13/2}$  level of  $\text{Er}^{3+}$  ions was realized both in  $\beta$ - and  $\alpha\text{-NaYF}_4$  NCs. Meanwhile, MIR fluorescence enhanced remarkably after calcination at high temperature. In comparison, A-NYF products with controllable morphology, smaller particle size, better uniformity and intense MIR emission present more possibility combining with glass to form NGC. During the calcination process, the phase transformation of  $\text{NaYF}_4$  between hexagonal and cubic phase was investigated in detail. The results show that as-prepared  $\beta\text{-NaYF}_4$  is located in stable state at low temperature, and transform into  $\alpha\text{-NaYF}_4$  upon  $\sim 600^\circ\text{C}$ , while as-prepared  $\alpha\text{-NaYF}_4$  transform into  $\beta\text{-NaYF}_4$  at low temperature, and then the  $\beta\text{-NaYF}_4$  transform back  $\alpha\text{-NaYF}_4$  upon  $\sim 600^\circ\text{C}$ . Further increase of temperature will result in oxidation of  $\text{NaYF}_4$ . Based on FTIR and PL spectra results, it can be deduced that the defect and crystallinity play a major role in MIR emission of  $\text{Er}^{3+}$  ions. Moreover, an interesting phenomenon attracts our attention, i.e. the MIR emission peak of  $\text{Er}^{3+}$  ions splits into three emission peaks in  $\alpha\text{-NaYF}_4$  NCs while there is only emission peak in  $\beta\text{-NaYF}_4$  NCs, which is due to the difference of site symmetry in both cubic and hexagonal phases. Although as-prepared  $\alpha\text{-NaYF}_4:5\%\text{Er}^{3+}$  NCs own spherical morphology and small size, bigger irregular nanoparticles are obtained on account of phase transformation after calcination, which will influence the compound properties of crystals. Hence, further investigation can be focused on suppressing phase transformation to control the morphology.

## Methods

**Preparation of  $\beta\text{-NaYF}_4:\text{Er}^{3+}$  NCs.**  $\beta\text{-NaYF}_4$  NCs doped with  $\text{Er}^{3+}$  ions were prepared using hydrothermal method based on oleic acid (OA 90 wt%, A.R.) as a stabilizing agent<sup>16</sup>. 1.4 g of NaOH (A.R.), 15 mL of OA, and 24.6 mL of  $\text{C}_2\text{H}_5\text{OH}$  (A.R.) were well mixed under stirring at room temperature to obtain a white viscous solution. 11.4 mL of 0.5 M  $\text{Y}(\text{NO}_3)_3$  and 0.6 mL of 0.2 M  $\text{Er}(\text{NO}_3)_3$  were added with vigorous stirring until a translucent solution was obtained. After 10 minutes of stirring, 12 mL of 1.0 M NaF solution was added dropwise into the above solution under vigorous stirring. After aging for 30 min, the mixture was transferred to a Teflon-lined 100 mL capacity autoclave, and heated at  $200^\circ\text{C}$  for 12 h. When the autoclave was air-cooled down to room temperature, the samples were washed alternately by deionized water and ethanol, and dried at  $80^\circ\text{C}$  for 8–12 h in air. Finally, the precursor powders were calcined at different temperatures for 2 h.

**Preparation of  $\alpha\text{-NaYF}_4:\text{Er}^{3+}$  NCs.** Monodisperse  $\alpha\text{-NaYF}_4:\text{Er}^{3+}$  spheres were prepared according to the literature with some modification<sup>42</sup>. In a typical synthesis, 9.5 mL of 0.2 M  $\text{Y}(\text{NO}_3)_3$  and 0.5 mL of 0.2 M  $\text{Er}(\text{NO}_3)_3$  were mixed with an aqueous solution of ethylenediamine tetraacetic acid disodium salt ( $\text{Na}_2\text{EDTA}$ , A.R.) under vigorous magnetic stirring to obtain a white complex. Afterwards, another solution of NaF (24 mmol added into 30 mL deionized water) was added into the above white solution and stirred for 1 h at room temperature. The as-obtained precipitates were centrifuged, washed several times with deionized water and ethanol, and then dried at  $80^\circ\text{C}$  for 8–12 h in air. Finally, the precursor powders were calcined at different temperatures for 2 h.

**Characterization.** The crystalline structure of  $\beta\text{-NaYF}_4:\text{Er}^{3+}$  and  $\alpha\text{-NaYF}_4:\text{Er}^{3+}$  NCs were investigated by X-ray diffraction (XRD) (Bruker, D8 ADVANCE analysis with Cu  $K\alpha$  radiation operated at 40 kV and 40 mA,  $\lambda = 0.15418$  nm, scanning step  $0.02^\circ$ , scanning speed 0.1 s per step). The morphology and size distribution of NCs were observed by field emission-scanning electron microscopy (FE-SEM, Nova NanoSEM403, FEI, Netherlands), and high-resolution transmission electron microscopy (HR-TEM, 2100F, JEOL, Japan) equipped with an energy-dispersive X-ray spectrometer (EDS). Thermal analysis of the precursor powders were detected by simultaneous thermal analyzer (STA, STA449C/3/MFC/GJUPITEY, NETZSCH, Germany). A heating rate of  $10^\circ\text{C}/\text{min}$  was adopted. The Raman spectra were measured using a Raman spectrometer (Renishaw in Via, Gloucestershire, UK) with a 532 nm laser as the excitation source. The organic groups in NCs were detected from Fourier transform-infrared spectroscopy (FT-IR, Vector-33, Bruker, Switzerland). The photoluminescence spectra were measured on a high resolution spectrofluorometer (Edinburgh Instruments FLS 920), which were excited by a 976 nm laser diode (LD).

## References

- Godard, A. Infrared (2–12  $\mu\text{m}$ ) solid-state laser sources: a review. *C. R. Phys.* **8**, 1100–1128 (2007).
- Sanamyan, T., Kanskar, M., Xiao, Y., Kedlaya, D. & Dubinskii, M. High power diode-pumped 2.7- $\mu\text{m}$   $\text{Er}^{3+}:\text{Y}_2\text{O}_3$  laser with nearly quantum defect-limited efficiency. *Opt. Express* **19**, A1082–A1087 (2011).

3. Zajac, A., Skorczakowski, M., Swiderski, J. & Nyga, P. Electrooptically Q-switched mid-infrared Er:YAG laser for medical applications. *Opt. Express* **12**, 5125–5130 (2004).
4. Wei, T. *et al.* Mid-infrared fluorescence, energy transfer process and rate equation analysis in Er<sup>3+</sup> doped germanate glass. *Sci. Rep.* **4** (2014).
5. Lu, Y. *et al.* Er<sup>3+</sup> doped germanate–tellurite glass for mid-infrared 2.7 μm fiber laser material. *J. Quant. Spectrosc. Ra.* **171**, 73–81 (2016).
6. Pollnau, M. & Jackson, S. D. In *Solid-State Mid-Infrared Laser Sources* 225–261 (Springer, 2003).
7. Seddon, A. B., Tang, Z., Furniss, D., Sujecki, S. & Benson, T. M. Progress in rare-earth-doped mid-infrared fiber lasers. *Opt. Express* **18**, 26704–26719 (2010).
8. Zhou, P., Wang, X., Ma, Y., Lü, H. & Liu, Z. Review on recent progress on mid-infrared fiber lasers. *Laser Phys.* **22**, 1744–1751 (2012).
9. Wang, F. *et al.* Tuning upconversion through energy migration in core–shell nanoparticles. *Nat. Mater.* **10**, 968–973 (2011).
10. Wang, F. *et al.* Simultaneous phase and size control of upconversion nanocrystals through lanthanide doping. *Nature* **463**, 1061–1065 (2010).
11. Chai, G., Dong, G., Qiu, J., Zhang, Q. & Yang, Z. 2.7 μm emission from transparent Er<sup>3+</sup>, Tm<sup>3+</sup> codoped yttrium aluminum garnet (Y<sub>3</sub>Al<sub>5</sub>O<sub>12</sub>) nanocrystals–tellurate glass composites by novel comelting technology. *J. Phys. Chem. C* **116**, 19941–19950 (2012).
12. Peng, J. *et al.* Optical Spectra and Gain Properties of Ho<sup>3+</sup>/Pr<sup>3+</sup> Co-doped LiYF<sub>4</sub> Crystal. *J. Mater. Sci. Technol.* **30**, 910–916 (2014).
13. He, H. *et al.* Controllable synthesis of Zn<sub>2</sub>GeO<sub>4</sub>:Eu nanocrystals with multi-color emission for white light-emitting diodes. *J. Mater. Chem. C* **3**, 5419–5429 (2015).
14. Secu, M. & Secu, C. Up-conversion luminescence of Er<sup>3+</sup>/Yb<sup>3+</sup> co-doped LiYF<sub>4</sub> nanocrystals in sol–gel derived oxyfluoride glass-ceramics. *J. Non-Cryst. Solids* **426**, 78–82 (2015).
15. Schäfer, H., Ptacek, P., Zerzouf, O. & Haase, M. Synthesis and optical properties of KYF<sub>4</sub>/Yb, Er nanocrystals, and their surface modification with undoped KYF<sub>4</sub>. *Adv. Funct. Mater.* **18**, 2913–2918 (2008).
16. Wang, F. & Liu, X. Recent advances in the chemistry of lanthanide-doped upconversion nanocrystals. *Chem. Soc. Rev.* **38**, 976–989 (2009).
17. Ding, M. Y. *et al.* Effect of heat-treatment temperature on upconversion luminescence of beta-NaYF<sub>4</sub>:Yb<sup>3+</sup>, Er<sup>3+</sup> nano/microparticles. *J. Inorg. Mater.* **28**, 146–152 (2013).
18. Zhang, F., Li, J., Shan, J., Xu, L. & Zhao, D. Shape, size, and phase-controlled rare-earth fluoride nanocrystals with optical up-conversion properties. *J. Chem. Eur.* **15**, 11010–11019 (2009).
19. Liu, X. *et al.* Optical gain at 1550 nm from colloidal solution of Er<sup>3+</sup>-Yb<sup>3+</sup> codoped NaYF<sub>4</sub> nanocubes. *Opt. express* **17**, 5885–5890 (2009).
20. Ma, Y. *et al.* Controllable synthesis and upconversion luminescence of NaYF<sub>4</sub>:Yb<sup>3+</sup>, Er<sup>3+</sup> nanocrystals. *Ceram. Int.* (2015).
21. Dong, G. *et al.* Morphology and phase control of fluorides nanocrystals activated by lanthanides with two-model luminescence properties. *Nanoscale* **4**, 4658–4666 (2012).
22. Chai, G., Dong, G., Qiu, J., Zhang, Q. & Yang, Z. Phase transformation and intense 2.7 μm emission from Er<sup>3+</sup> doped YF<sub>3</sub>/YOF submicron-crystals. *Sci. Rep.* **3** (2013).
23. Ichikawa, M., Ishikawa, Y.-i., Wakasugi, T. & Kadono, K. Mid-infrared emissions from Ho<sup>3+</sup> in Ga<sub>2</sub>S<sub>3</sub>-GeS<sub>2</sub>-Sb<sub>2</sub>S<sub>3</sub> glass. *J. Lumin* **132**, 784–788 (2012).
24. Ren, J. *et al.* Intense near-infrared and midinfrared luminescence from the Dy<sup>3+</sup>-doped GeSe<sub>2</sub>-Ga<sub>2</sub>Se<sub>3</sub>-MI (M = K, Cs, Ag) chalcogenide glasses at 1.32, 1.73, and 2.67 μm. *J. Appl. Phys.* **109**, 033105 (2011).
25. Guo, Y., Li, M., Hu, L. & Zhang, J. Effect of fluorine ions on 2.7 μm emission in Er<sup>3+</sup>/Nd<sup>3+</sup>-codoped fluorotellurite glass. *J. Phys. Chem. A* **116**, 5571–5576 (2012).
26. Xu, R., Tian, Y., Hu, L. & Zhang, J. Enhanced emission of 2.7 μm pumped by laser diode from Er<sup>3+</sup>/Pr<sup>3+</sup>-codoped germanate glasses. *Opt. Lett.* **36**, 1173–1175 (2011).
27. Wu, G. *et al.* 2.7 μm emission in Er<sup>3+</sup>:CaF<sub>2</sub> nanocrystals embedded oxyfluoride glass ceramics. *Opt. Lett.* **38**, 3071–3074 (2013).
28. Wei, T. *et al.* 2.7 μm emissions in Er<sup>3+</sup>:NaYF<sub>4</sub> embedded aluminosilicate glass ceramics. *Ceram. Int.* **42**, 1332–1338 (2016).
29. Wang, P. *et al.* Concentration effect of Nd<sup>3+</sup> ion on the spectroscopic properties of Er<sup>3+</sup>/Nd<sup>3+</sup> co-doped LiYF<sub>4</sub> single crystal. *Mater. Chem. Phys.* **144**, 349–354 (2014).
30. Assaoudi, H., Shan, G.-B., Dyck, N. & Demopoulos, G. P. Annealing-induced ultra-efficient NIR-to-VIS upconversion of nano-/micro-scale α and β NaYF<sub>4</sub>:Er<sup>3+</sup>, Yb<sup>3+</sup> crystals. *Cryst Eng Comm* **15**, 4739–4746 (2013).
31. Wang, G. *et al.* Controlled synthesis and luminescence properties from cubic to hexagonal NaYF<sub>4</sub>:Ln<sup>3+</sup> (Ln = Eu and Yb/Tm) microcrystals. *J. Alloy. Compd.* **475**, 452–455 (2009).
32. Renero-Lecuna, C. *et al.* Origin of the high upconversion green luminescence efficiency in β-NaYF<sub>4</sub>:2% Er<sup>3+</sup>, 20% Yb<sup>3+</sup>. *Chem. Mater.* **23**, 3442–3448 (2011).
33. Luo, X. & Akimoto, K. Upconversion properties in hexagonal-phase NaYF<sub>4</sub>:Er<sup>3+</sup>/NaYF<sub>4</sub> nanocrystals by off-resonant excitation. *Appl. Surf. Sci.* **273**, 257–260 (2013).
34. Zhang, Y. *et al.* YOF nano/micro-crystals: morphology controlled hydrothermal synthesis and luminescence properties. *Cryst Eng Comm* **16**, 2196–2204 (2014).
35. Lixin, Y., Hongwei, S., Zhongxin, L., Linmei, Y. & Zheng, S. L. Z. Electronic transition and energy transfer processes in LaPO<sub>4</sub>-Ce<sup>3+</sup>/Tb<sup>3+</sup> nanowires. *J. Phys. Chem. B* **109**, 11450–11455 (2005).
36. Zhang, X., Zhang, J., Ren, X. & Wang, X.-J. The dependence of persistent phosphorescence on annealing temperatures in CaTiO<sub>3</sub>:Pr<sup>3+</sup> nanoparticles prepared by a coprecipitation technique. *J. Solid State Chem.* **181**, 393–398 (2008).
37. Dantelle, G., Mortier, M. & Vivien, D. EPR and optical studies of erbium-doped β-PbF<sub>2</sub> single-crystals and nanocrystals in transparent glass-ceramics. *Phys. Chem. Chem. Phys.* **9**, 5591–5598 (2007).
38. Tikhomirov, V. K. *et al.* Er<sup>3+</sup>-doped nanoparticles for optical detection of magnetic field. *Nano Lett.* **9**, 721–724 (2009).
39. Steinkemper, H., Fischer, S., Hermle, M. & Goldschmidt, J. Stark level analysis of the spectral line shape of electronic transitions in rare earth ions embedded in host crystals. *New J. Phys.* **15**, 053033 (2013).
40. Chen, P. *et al.* Lanthanide doped nanoparticles as remote sensors for magnetic fields. *Nanoscale* **6**, 11002–11006 (2014).
41. Zhang, Y. *et al.* Simultaneous luminescence modulation and magnetic field detection via magneto-optical response of Eu<sup>3+</sup>-doped NaGdF<sub>4</sub> nanocrystals. *J. Mater. Chem. C* **3**, 10140–10145 (2015).
42. He, F. *et al.* Influence of surfactants on the morphology, upconversion emission, and magnetic properties of β-NaGdF<sub>4</sub>:Yb<sup>3+</sup>, Ln<sup>3+</sup> (Ln = Er, Tm, Ho). *Dalton Trans.* **42**, 10019–10028 (2013).

## Acknowledgements

This work has been supported by the National Natural Science Foundation of China (61475047, 51302086); Guangdong Natural Science Foundation for Distinguished Young Scholars (2014A030306045); Pearl River S&T Nova Program of Guangzhou (2014J2200083); West Light Foundation from Chinese Academy of Science (CAS) of China, and the Fundamental Research Funds for the Central Universities (2015PT021).

### Author Contributions

G.D. proposed and guided the overall project. D.Y, H.H., Q.P. and Q.X. performed all the experiments and analyzed the results. All the authors discussed the results. D.Y. and G.D. wrote the manuscript, with discussion from D.C. and J.Q.

### Additional Information

**Supplementary information** accompanies this paper at <http://www.nature.com/srep>

**Competing financial interests:** The authors declare no competing financial interests.

**How to cite this article:** Yang, D. *et al.* Controllable Phase Transformation and Mid-infrared Emission from Er<sup>3+</sup>-Doped Hexagonal-/Cubic-NaYF<sub>4</sub> Nanocrystals. *Sci. Rep.* **6**, 29871; doi: 10.1038/srep29871 (2016).



This work is licensed under a Creative Commons Attribution 4.0 International License. The images or other third party material in this article are included in the article's Creative Commons license, unless indicated otherwise in the credit line; if the material is not included under the Creative Commons license, users will need to obtain permission from the license holder to reproduce the material. To view a copy of this license, visit <http://creativecommons.org/licenses/by/4.0/>